Manuscript submitted to
AIMS' Journals
Volume , Number **0**,

Website: http://AIMsciences.org

pp. **000–000**

MEASURING THE TOTAL AMOUNT OF CHAOS IN SOME HAMILTONIAN SYSTEMS

Carles Simó

Departament de Matemàtica Aplicada i Anàlisi
Universitat de Barcelona
Gran Via 585, 08007 Barcelona, Catalunya

(Communicated by)

Abstract. We consider some simple Hamiltonian systems, variants or generalizations of the Hénon-Heiles system, in two and three degrees of freedom, around a positive definite elliptic point, in resonant and non-resonant cases. After reviewing some theoretical background, we determine a measure of the domain of chaoticity by looking at the frequency of positive Lyapunov exponents in a sample of initial conditions. The question we study is how this measure depends on the energy and parameters and which are the dynamical objects responsible for the observed behaviour.

To the memory of Michel Hénon (1931–2013),
a pioneer introducing paradigmatic models.

1. **Introduction.** Many phenomena are described using a Hamiltonian formulation. Integrable Hamiltonian systems are, for some problems, interesting approximations, which allow to guess some of the properties of the studied problem. There are several tools to detect the lack of integrability of such a system, either based on an algebraic approach, see Section 2.1, or based on numerical evidences obtained from simulations, see Section 3.

But one of the key points is to have some quantitative information on the amount of chaos to be found in a given system, providing a measure on how far it is from integrable. It is relevant because if that amount is very small, below some threshold, it can be neglected and the system can be considered as integrable for practical applications. A related topic is that despite the amount of chaos can be important, perhaps it takes a very large time to show up, even longer than the time of validity of the model.

At that point there are crucial questions:

- Which are the dynamical objects responsible for the chaos?
- Can they be detected and measured in some reasonable way, to be able to predict the amount of chaos of the system?

2000 *Mathematics Subject Classification.* Primary: 70H07, 70K70 ; Secondary: 34D08, 37J40, 37J45, 37M25.

Key words and phrases. measures of chaos, Hamiltonian systems, splitting of invariant manifolds.

- How do the answers to these questions depend on the level of energy and on the parameters of the system?

In this work we present an approach to that topic, giving some answers and suggesting several open problems.

In Section 2 we recall some quite well know theoretical facts, looking at the algebraic aspects of integrability and at the regular motions which follow from KAM theory.

Section 3 is devoted to describe some of the algorithms used to detect the fraction of the phase space which can be considered that has chaotic behaviour.

Section 4 presents some simple examples, the first one being the classical Hénon-Heiles Hamiltonian [15]. Other examples are based on variants of this model or generalizations to 3 degrees of freedom (dof). For simplicity we consider the system in the vicinity of a totally elliptic fixed point, with positive definite quadratic part, and we restrict the study to values of the energy such that there is a compact component of that energy level. After every example we try to give a theoretical support to explain the observed behaviour, identifying the related dynamical objects and making a quantitative analysis.

In all the presentation the systems are assumed to be analytical.

2. **A review of some theoretical background.**

Let us consider a Hamiltonian $H(q,p)$ with n degrees of freedom (dof), where (q,p) belong to some domain in $\mathbb{R}^{2n}$ or, in some cases, in $\mathbb{T}^n \times \mathbb{R}^n$. We refer to standard books [1, 29, 33] for basic definition and facts. The dynamics is described by

$$\frac{dq_j}{dt} = \frac{\partial H}{\partial p_j}(q,p), \quad \frac{dp_j}{dt} = -\frac{\partial H}{\partial q_j}(q,p), \quad j = 1,\dots,n. \tag{1}$$

Let F be a first integral of the system which makes zero the Poisson bracket

$$\{F,H\} = \sum_{j=0}^{n} \left(\frac{\partial F}{\partial q_j}\frac{\partial H}{\partial p_j} - \frac{\partial F}{\partial p_j}\frac{\partial H}{\partial q_j} \right). \tag{2}$$

We recall that two functions F, G are said to be in involution if $\{F,G\} = 0$. A system is said to be integrable in the Liouville-Arnold sense if it has n first integrals $F_1,\dots,F_n$, in involution, and functionally independent almost everywhere. In case the joint level of the first integrals $F_1^{-1}(c_1) \cap \dots F_1^{-1}(c_n)$ is compact, for some values of $c_1,\dots,c_n$, a celebrated theorem by Arnold ensures that it is diffeomorphic to $\mathbb{T}^n$.

2.1. **Algebraic detection of the lack of integrability.**

There exist several algebraic tools to detect the lack of integrability of a system like (1). The basic idea is to derive necessary conditions for integrability and then to check that some of these conditions fail. One can look at [23] as standard reference.

The starting point is to consider a solution of (1) of the form $z(t)$, but looking at t as a complex variable. Then z defines a Riemann surface Γ and we can consider the first variational equations, VE1, associated to (1), say $\dot{\xi} = A(t)\xi$, when $z(t)$ moves along a path γ in Γ.

A first general approach was derived by Ziglin [45], looking at the monodromy matrices, i.e., the solutions in matrix form of the VE1, using different paths γ_1, γ_2. If we denote as M_1 and M_2 these matrices, a necessary condition for the integrability is that they commute.

This was extended on the line of Picard-Vessiot theory. See, e.g., [27] for one of the preliminary works in this direction. In the VE1 the entries in $A(t)$ belong

to some field of (meromorphic) functions K (depending on the equations of the problem and on the selected solution). But, in general, the entries of a fundamental matrix M of the VE1 belong to a larger field of functions, L, which can be seen as an extension of K obtained by adjunction of the entries of M (if not in K). This leads, in a natural way, to consider the Galois group G of the extension L/K, which is an algebraic group. The key result, see [24, 25], tells us that a necessary condition for integrability is that the identity component G^0 (in the Zariski topology) of the Galois group G must be commutative. See the above references for technical details.

Finally, the previous result was extended, see [26], to the case in which G^0 turns out to be commutative and, hence, it is not producing any obstruction to integrability. To this end one can consider not only the VE1 but the variational equations to order $m > 1$, VEm or, in other words, the jet up to order m of the solution as a function of the initial conditions. The system of VEm is not linear, but it can be reduced to the study of a linear system by including some additional variables, see [26]. Then, in a completely analogous way, one derives a necessary condition for integrability involving the variational equations along paths γ in Γ up to order m. A generalized Galois group, G_m, must have a commutative identity component $(G_m)^0$. Alternatively, one can require the commutativity, up to order m, of the propagation of the jets along paths on Γ. Note that even in the case $(G_m)^0$ commutative for all $m \geq 1$, one can not claim that H is integrable.

The Hénon-Heiles system to be studied in Section 4.1 leads in a natural way to study a one-parameter family of 2 dof Hamiltonian systems. Ito [16] proved that all of them, including the original system, are non-integrable by using Ziglin's result, except for 4 values of the parameter. For three of these values the systems have been proved to be integrable. The fourth one was proved to be non-integrable using VE3 (see [26]). See [20] for methodology and other examples on the use of higher order variational equations and [21] for a delicate case involving different singularities.

The main problem of the algebraic approach is that, up to now, it does not offer any quantitative information on some measure of the amount of chaos to be expected on a given system.

2.2. **KAM theory.** Consider now an integrable system for which the levels of the n integrals $F_1, \ldots, F_n$ are tori. Then it is possible to introduce angle-action variables $(\varphi, I) \in \mathbb{T}^n \times U$, $U \subset \mathbb{R}^n$ and, in these variables, the Hamiltonian can be written simply as $H_0(I)$. Hence, it can be integrated explicitly, giving $I =$ctant, $\varphi(t) = \varphi(0) + t\omega(I)$, where $\omega(I) = \nabla(H_0(I))$ denotes the frequency vector. Therefore, there are domains in which the phase space is foliated by invariant tori and, in these tori, the dynamics is quasiperiodic if $\omega(I)$ is non-resonant, that is, if one has $(k, \omega(I)) \neq 0$ for all $k \in \mathbb{Z}^n \setminus \{0\}$.

The standing question is what happens when the system is perturbed to a new Hamiltonian $H(\varphi, I, \varepsilon) = H_0(I) + \varepsilon H_1(\varphi, I, \varepsilon)$. The celebrated KAM theorem, see for instance [1, 29, 33], tells us that the previous tori subsist, with a small deformation, provided three conditions hold:

- The frequencies satisfy a Diophantine condition:
$$|(k, \omega)| \geq c/|k|^\tau \quad \text{for all} \quad k \in \mathbb{Z}^n \setminus \{0\}, \tag{3}$$
for some $c > 0, \tau > 0$ (in fact it should be $\tau \geq n - 1$), being $|k|$ a norm of k.
- The unperturbed Hamiltonian satisfies a non-degeneracy condition, which amounts to require that the passage from I to $\omega(I)$ is invertible: $\mathrm{Hess}(H_0(I))$ must be a regular matrix. This is called the torsion condition.

- The value of the perturbation parameter ε is sufficiently small.

It should be clear that the conditions are related in some way. Having a strong torsion can help to keep the tori if ε increases or if c decreases (for a fixed τ) in the Diophantine condition.

Furthermore, one can ask which will be the measure of the set of points which were in tori for $\varepsilon = 0$ and such that the tori have been destroyed due to the perturbation. Typically one expects to have a measure $\mathcal{O}(\varepsilon^{1/2})$, assuming that the torsion condition is satisfied in all the domain under consideration. This follows from an estimate of the measure of the resonant domains, close to the hypersurfaces in the action space, for which $(k, \omega(I)) = 0$ for some $k \in \mathbb{Z}^n \setminus \{0\}$. However one can expect to have $\mathrm{Hess}(H_0(I))$ singular around some hypersurfaces in the action space. This will change the exponent $1/2$ of ε to smaller values, giving, in principle, a domain with larger measure without KAM tori.

But in the complement of the KAM tori can appear satellite tori which can fill an important part of the measure previously excluded. This will be illustrated in several of the examples in Section 4.

The KAM results apply to symplectic maps. An integrable symplectic map in dimension $2n$ is obtained as Poincaré section, on a given level of energy, of an integrable Hamiltonian with $n+1$ dof or as the time-1 flow of an integrable Hamiltonian with n dof. Under suitable conditions, most of the tori of the unperturbed symplectic map are preserved (slightly deformed) under perturbation.

A particular case, relevant when studying Hamiltonian systems with 2 dof, are the two-dimensional (2D) symplectic maps. A simple model are the so-called twist maps, of the form $(\varphi, I) \mapsto (\varphi + \alpha(I), I)$, where $(\varphi, I) \in \mathbb{S} \times [a, b]$ for a fixed interval $[a, b]$. The radius depending rotation $\alpha(I)$ is asked to satisfy the twist condition $d\alpha(I)/dI \neq 0$. Then, Moser theorem ensures the preservation of invariant circles having Diophantine rotation number for sufficiently small perturbations.

But if $d\alpha(I)/dI(I^*) = 0$ for some $a < I^* < b$, some more complicated patterns can appear, depending on the degree of degeneracy of α at I^*. In the generic case $d^2\alpha(I)/dI^2(I^*) \neq 0$ the so-called meandering curves [36] appear and they fill up most of the domain not covered by the KAM invariant curves (despite the existence of meandering curves also follows from KAM theorem).

3. **Tools for detecting chaos and related topics.** Faced to a given Hamiltonian there are different tools to detect, for given initial conditions, whether the corresponding orbit can be considered regular or chaotic. They are mainly based on the so-called frequency analysis and on the estimates of Lyapunov exponents or some related quantity. We refer to [37] for an overview and different examples.

Frequency analysis is a very popular tool since the systematic use made by Laskar [17] for the study of the solar system. The key idea is to try to determine that a given orbit can be assumed to be quasiperiodic for a given time interval $[0, T_1]$ and to obtain a basis of the frequencies. The computation is repeated for another interval $[T_2, T_3]$, $T_2 \geq T_1$ and then one checks if one can accept that the basis coincides with the previous one within a prescribed tolerance. There are effective algorithms to check for the quasiperiodicity of the orbit or to detect that the assumption is wrong. We refer to [13, 14] for an efficient methodology, several examples and the theoretical background. A very accurate and fast method has been recently introduced in [19].

Another approach, in cases that can be reduced to check for a discrete map if the orbit of an initial point is quasiperiodic in an invariant curve, is purely topological and based on the order of the successive iterates. One can look at the appendix in [32], where it has been applied to 2D tori of partial differential equations. It will be used in Section 4.3.

3.1. **Direct estimates of Lyapunov exponents.** A widely used method to detect chaos is to obtain estimates of the maximal Lyapunov exponent, that is, the exponential rate of divergence of nearby orbits. This was, essentially, the method used in the Hénon-Heiles paper [15]. One should mention, however, that while regular orbits have zero Lyapunov exponents, the converse is not true, despite can be seen as exceptional. For simplicity we sketch the method in the case of discrete maps (either conservative or not).

Let x_0 be an initial point and $x_0, \ldots, x_n, \ldots$ the orbit under a map F: $x_{k+1} = F(x_k)$. Let v_0 be a random unitary vector. We compute normalized images, v_k, of v_0 and the related Lyapunov sums LS_k for $k \geq 1$, starting with $LS_0 = 0$, as follows:

$$w_k = DF(x_{k-1})v_{k-1},\ v_k = \frac{w_k}{||w_k||_2},\ LS_k = LS_{k-1} + \log(||w_k||_2),\ x_k = F(x_{k-1}). \quad (4)$$

The maximal Lyapunov exponent Λ, if it exists, will be found, with probability 1, as the limit slope of LS_k as a function of k. If F comes from the passage through a Poincaré section Σ, the values of LS_k should be considered as a function of the passage times t_k through Σ.

The problem is how to decide to stop the computation. A possible solution is to look for the slope of a fit of LS_k as a function of k after N iterates, using different fractions of the sample (say, last 70%, last 50% and last 30%) and accept the estimated values if they differ in less than a prescribed tolerance. Otherwise the computation is continued up to $2N, 3N, \ldots$ iterates without exceeding a given maximum. And an additional problem, if we are interested in deciding if the dynamics can be considered regular or chaotic, is to set up a threshold on the estimated Λ to consider the orbit as chaotic. Typically this is guided by some preliminary tests.

However, if we are only interested in deciding if the dynamics is regular or chaotic, there are shortcuts. For regular orbits the behaviour of the norm of v_k (without the scaling in (4)) is typically linear in k. For an integrable Hamiltonian system with vector field X^H, the integration of the VE1 $d\xi/dt = DX^H(t)\xi$ gives, generically, a linear behaviour for the norm of $\xi(t)$ as a function of t (with superimposed quasiperiodic oscillations), the coefficient of the linear part being related to the torsion. Hence, if we accept that the linear part has a coefficient bounded by κ and after some transient one has $LS_k > \log(\kappa k)$, one can consider that the orbit is chaotic.

3.2. **MEGNO.** As it has been mentioned, in the regular case there are quasiperiodic oscillations and, furthermore, if LS_k behaves as $\log(k)$ because of the linear terms (or $LS(t)$ as $\log(t)$ in the continuous case) the convergence of the linear fits to zero is slow. A methodology was proposed and used in [3] to filter the oscillations and speed up the convergence.

A systematic methodology, for conservative systems, with fast convergence was introduced in [4], where a weighted formulation was presented to study the Mean Exponential Growth factor of Nearby Orbits (MEGNO). It turns out to be very efficient when interested on the concrete value of Λ. See [18] for an example of a systematic massive application where the object of study was the metric entropy of

a discrete map as a function of a parameter. We recall that the metric entropy can be recovered by integration of the Lyapunov exponent according to Pesin's theory [31].

Again, if we are only interested in deciding between regular or chaotic, a shortcut used in the examples in Section 4 proceeds as follows. Let us denote as z the variables in the Hamiltonian formulation, as X^H the Hamiltonian vector field and as ζ the variable in the first variational equations. We add an equation for an extra variable Y

$$\frac{dz}{dt} = X^H(z), \quad \frac{d\zeta}{dt} = DX^H(z(t))\zeta, \quad \frac{dY}{dt} = t\frac{(d\zeta/dt, \zeta)}{(\zeta, \zeta)}. \tag{5}$$

Then the value of $Y(t)/t$ tends to 1 for regular orbits, while it is divergent for chaotic ones. Hence, one can compute $Y(t)$ up to some time T and check if it is below Tc_1 with c_1 a little bit greater than 1, or larger than Tc_2 with c_2 away from 1. In the first case the dynamics is considered as regular and in the second one as chaotic. For values $Tc_1 \le Y(T) \le Tc_2$ one can continue up to a larger time. This, together with the checks on the values of $LS(t)$ described in Section 3.1, has been efficiently used in Section 4 where system (5) is integrated using high order Taylor methods.

3.3. **Detecting very small positive Lyapunov exponents.** A critical case appears when the system under study has a large fraction of chaotic motion but the related Lyapunov exponents are rather small. This will appear in Section 4.4 where a generalization of the Hénon-Heiles system to a 3 dof Hamiltonian in 1:1:1 resonance is studied. A direct approach is extremely time consuming. But using a suitable scaling of variables, a few steps of normal form, averaging and time scaling, makes the computations quite easy. Details will be given in Section 4.4.

4. **Examples: numerical results and theoretical explanations.** As already mentioned in this Section we study a few simple examples around a totally elliptic fixed point, for two and three degrees of freedom, with resonant and non-resonant frequencies at the fixed point.

Before proceeding to describe the results we can comment on the sampling. That is, how the initial conditions have been taken on a given level of the energy. In the case of 2 dof a simple method consists in taking a grid on a Poincaré section, but one can also take initial conditions in an approximately equispaced grid on the full level, close to $\mathbb{S}^3$ for small energies. In the case of 3 dof one can also take points on a grid in a Poincaré section, or in an approximately equispaced grid in $\mathbb{S}^5$. But because of the form of the Hamiltonian functions used for 3 dof, one can take points on a level $H^{-1}(h)$ with zero velocity: $p_x = p_y = p_z = 0$. The results are slightly different, depending on the method and on the number of points in the grids (ranging, roughly, from 10^5 for h such that there is a big amount of chaos, to 10^7 when few orbits are chaotic). But the global trends, as a function of h, are identical.

4.1. **The classical Hénon-Heiles Hamiltonian.** The first example is the celebrated Hénon-Heiles system, a model of the dynamics of stars in galaxies with cylindrical symmetry and that provided strong numerical evidence of the lack of first integrals beyond the energy. It is given by

$$H(x, y, p_x, p_y) = \frac{1}{2}(x^2 + y^2 + p_x^2 + p_y^2) + x^3/3 - xy^2, \tag{6}$$

and it has bounded components of $H^{-1}(h)$ until $h = 1/6$. Figure 1 shows a plot of the Poincaré map $\mathcal{P}$ on the section $y = 0, p_y > 0$ on the level $h = 0.1$. The system has 8 simple periodic orbits (p.o.), 5 of them elliptic and 3 hyperbolic. Four of the elliptic p.o. are seen on the plot, surrounded by invariant curves, while the fifth one lies at the boundary and, hence, $\mathcal{P}$ is not defined on it. The three hyperbolic p.o. are marked as green points and are seen to be surrounded by chaotic domains.

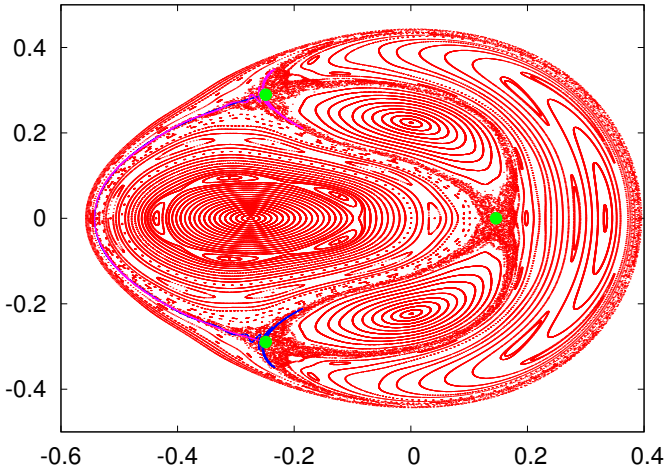

FIGURE 1. Poincaré map $\mathcal{P}$ related to (6) on the level $H^{-1}(0.1)$. The coordinates displayed are (x, p_x). See the text for details.

4.1.1. *Numerical results.* The three hyperbolic fixed points of $\mathcal{P}$ give rise to heteroclinic connections. In the Figure 1 we also display the left branch of the unstable manifold W^u_+ of the left upper fixed point (in blue) and the left branch of the stable manifold W^s_- of the left lower fixed point (in magenta). Because of the symmetry $S : (x, p_x) \leftrightarrow (x, -p_x)$ one has $S(W^u_+) = W^s_-$ and an heteroclinic point lies on $p_x = 0$. Note that, despite h is not close to zero, it is hard to distinguish W^u_+ from W^s_- near $p_x = 0$ but it becomes easier close to the fixed points.

Using the methods described in Section 3 the fraction of regular points

$$\psi(h) = \frac{\text{points considered regular in } H^{-1}(h)}{\text{total number of tested points in } H^{-1}(h)} \tag{7}$$

has been computed. The results are shown in Figure 2. On the left plot the value of $\psi(h)$ as a function of h is displayed. One can see that for $h = 0.07$ it seems that most of the dynamics is regular. In fact, for $h = 0.06$ the chaotic fraction is only a little bit larger than 10^{-6}. The right plot displays $h \log(1 - \psi(h))$ also as a function of h and a fit by a function of the form

$$\ell(h) = ah + bh \log(h) - c \tag{8}$$

with respect to the parameters a, b, c. Let us denote as a_c, b_c, c_c the values obtained in the fit, to stress that they refer to the measure of the chaotic domain. The reasons to select the plotted function and the fitting function ℓ will be clear in what follows. Some of the irregularities that one can see in Figure 2 left, for not so small values of h, have a clear explanation. The sudden decrease in $\psi(h)$ close to $h = 0.12$ is due to the following. In Figure 1 one can see 5-periodic islands around the elliptic fixed point on $x < 0, p_x = 0$. Increasing h the associated hyperbolic 5-periodic points

create a chaotic zone which quickly increases just below $h = 0.12$ and then it merges with the largest chaotic zone associated to the fixed hyperbolic points. See [22] for a detailed study in the case of the Hénon map, which allows to identify most of the irregularities in functions like $\psi(h)$.

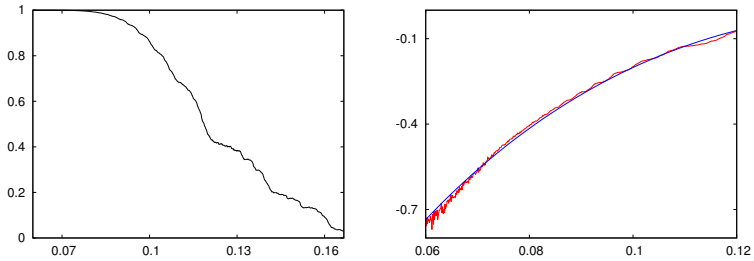

FIGURE 2. Left: The fraction $\psi(h)$ of regular dynamics, see (7), as a function of h. Right: the function $h\log(1-\psi(h))$ also as a function of h. In blue the fit by a function as in (8).

We want to compare the results displayed in Figure 2 with the splitting of the branches W^u_+ and W^s_-, given by the angle between them at the first intersection with $p_x = 0$ on $x < 0$, as seen in Figure 1. To this end we compute the branch W^u_+, the heteroclinic point and the tangent vector to W^u_+ as described in [34]. The results are shown in Figure 3. In the left plot we show the splitting angle $\sigma(h)$ as a function of the energy. It goes quickly to zero when h decreases. In the middle plot we show the values of $h\log(\sigma(h))$, also as a function of h, in an intermediate range, excluding values of h for which $\sigma(h)$ is too small to be confident on the values computed in double precision, and large values of h, for which the destruction of invariant curves around 5-periodic orbits plays an additional role, as commented before. We also plot, in blue, a fit of the data using a function ℓ as given in (8). In the right plot we display the same data $h\log(1-\psi(h))$ shown in Figure 2 right and a modification of the last fit, by changing the values of a and b. For concreteness we denote now the fitting values as a_s, b_s, c_s, to stress that they refer to the fit of the splitting. The agreement is excellent.

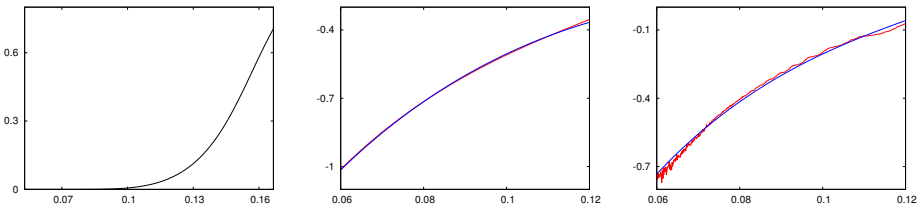

FIGURE 3. Left: The splitting angle $\sigma(h)$ between W^u_+ and W^s_- as a function of h. Middle: $h\log(\sigma(h))$ is plotted vs h and a fit by a function like (8) is plotted in blue. Right: The data in Figure 2 right and a minor modification of the fit in the middle part.

4.1.2. *Theoretical support.* First we present some preliminaries which will be also used in other examples. Introducing the scaling

$$x = \nu X,\ y = \nu Y,\ p_x = \nu P_X,\ p_y = \nu P_Y \tag{9}$$

in the system coming from (6) and setting $h = \nu^2/2$, it is clear that to study the dynamics of (6) is equivalent to look at the level $H = 1/2$ putting ν in front of the cubic terms. With this scaling the level of energy is close to the unit sphere $\mathbb{S}^3$ and tends to it when $\nu \to 0$. Furthermore for $\nu = 0$ the Poincaré map $\mathcal{P}$ is the identity.

Hence, for small ν the map $\mathcal{P}$ will be a close to the identity map, except near the boundary where $\mathcal{P}$ is not defined. This can be easily remedied by compactifying the disk to $\mathbb{S}^2$, identifying all the points at the boundary. This leads us to consider (analytical) maps close to the identity.

Consider, in general, a near the identity map $F_\varepsilon : z \mapsto z + \varepsilon F(z)$. Then, if ε is sufficiently small, it can be realized as the time-1 map of a vector field $\varepsilon f(z, t, \varepsilon)$, 1-periodic in t, known as a suspension. Neishtadt's averaging theorem [30] allows to reduce it to an autonomous vector field $g(z)$ plus a remainder with a bound of the form $a \exp(-c/\varepsilon)$ for some $a, c > 0$, by selecting the optimal order of averaging. See [2] for an example on the use of this idea. For bounds on averaging in the case in which the dependence in t is quasiperiodic, say $\dot z = \varepsilon f(z, \theta, \varepsilon)$, $\dot\theta = \omega \in \mathbb{R}^d$, with frequencies ω satisfying (3), see [35]. For upper and lower bounds, when there is a strong control on the perturbation, see [5]. Note that in the quasiperiodic case one requires also analyticity of f wrt θ. This is not at all needed in the periodic case.

If the family of maps F_ε is 2D symplectic then the averaged field g is Hamiltonian and it is possible to be more precise. Assume g has a hyperbolic fixed point P having a separatrix. We assume the time is normalized so that the dominant eigenvalue of $Dg(P)$ is equal to 1. Let $\beta(t)$ be the solution corresponding to this separatrix: $\lim_{t\to\pm\infty} \beta(t) = P$. Let ρ be such that β is analytical for $|\mathrm{Im}(t)| < \rho$. The family of symplectic 2D maps $F_\varepsilon : z \mapsto z + \varepsilon F(z)$ will have associated hyperbolic fixed points P_ε whose invariant manifolds are close to the separatrix β, see [7], but generically they do not coincide. Then, given a small fixed value η, it is possible to derive a general upper bound for any measure $\mu(\varepsilon)$ of the splitting (like the angle at an homoclinic point) of the form

$$\mu(\varepsilon) < A \exp\left(-\frac{2\pi(\rho - \eta)}{\zeta(\varepsilon))}\right), \tag{10}$$

where $\zeta(\varepsilon) = \log(\lambda(\varepsilon))$, being $\lambda(\varepsilon)$ the dominant eigenvalue of F_ε at P_ε. See [8] for the details and [10] for additional information, several examples and the role of the location of the singularities of β. We also refer to [10] for the methodology to compute invariant manifolds and splitting for these problems.

It is relevant to note that expressions like (10) provide not only upper bounds but, in many cases, the correct asymptotic estimates of $\mu(\varepsilon)$ if the singularities of β are located at $\pm\rho\,\mathrm{i}$. These estimates are of the form

$$A\varepsilon^B \exp(-2\pi\rho/\zeta(\varepsilon))(1 + o(1)) \tag{11}$$

for suitable A, B. This is the reason which leads to use a fitting function like (8) in the middle plot of Figure 3. Note that in that case the measure μ is replaced by the angle σ and that the log of the dominant eigenvalue is $\mathcal{O}(h)$ (h being here the energy), as it follows from a simple normal form computation.

But singularities located at $\pm\rho\,\mathrm{i} \pm \delta$ can give asymptotic estimates like

$$A\varepsilon^B \exp(-2\pi\rho/\zeta(\varepsilon))(\cos(2\pi\delta/\zeta(\varepsilon) + \varphi(\varepsilon)) + o(1)) \tag{12}$$

or even more complex. Here $\varphi(\varepsilon)$ denotes some suitable phase. See [10] for several examples in this direction. This will be the case in Section 4.2.

Remark. As all these estimates come from computing the relative positions of the manifold in a fundamental domain, say $W^u(P_\varepsilon)$ wrt $W^s(P_\varepsilon)$, this amounts to obtain the Fourier coefficients of that relative position. It can happen that, due to a symmetry, some of the harmonics which come from a singularity of β cancel and the dominant terms in the splitting come from singularities which are not the closest ones to the real axis.

Up to now we have presented the theoretical support for the behaviour of the splitting. Why the chaotic fraction has a similar behaviour in this example?

To this end one should introduce the 2D separatrix map. As a guiding example Figure 4 shows the manifolds of a hyperbolic fixed point A, which will appear in Section 4.2, in the (x, p_x) variables and a detail of the upper part. The splitting of the manifolds is clearly seen, but for the limit Hamiltonian flow they coincide. Consider a strip, $\mathcal{D}_+$ around that limit separatrix, between the sections labeled I and J, corresponding to homoclinic points with $J = \mathcal{P}(I)$. The separatrix map describes the return to $\mathcal{D}_+$ after passing close to A (eventually it returns to a similar domain $\mathcal{D}_-$ in $p_x < 0$). Using in $\mathcal{D}_+$ coordinates ξ, like an angle increasing from 0 to 2π when going from I to J, and η, transversal to the limit separatrix, equal to zero on W^s and positive inside the loop, and similar coordinates in $\mathcal{D}_-$, the simplest formulation for the separatrix map is

$$SepM : \begin{pmatrix} \xi \\ \eta \\ s \end{pmatrix} \to \begin{pmatrix} \bar\xi = \xi + c - \log(|\bar\eta|)/\zeta \ (\mathrm{mod}\ 2\pi) \\ \bar\eta = \eta + \mu \sin(\xi) \\ \bar s = s \times \mathrm{sign}(\bar\eta) \end{pmatrix}, \tag{13}$$

where s is a sign, to denote if the point belongs to $\mathcal{D}_+$ or to $\mathcal{D}_-$, μ is a measure of the splitting (typically the maximum distance between W^u and W^s in the fundamental domain), ζ is the log of the dominant eigenvalue at A and c an additive constant.

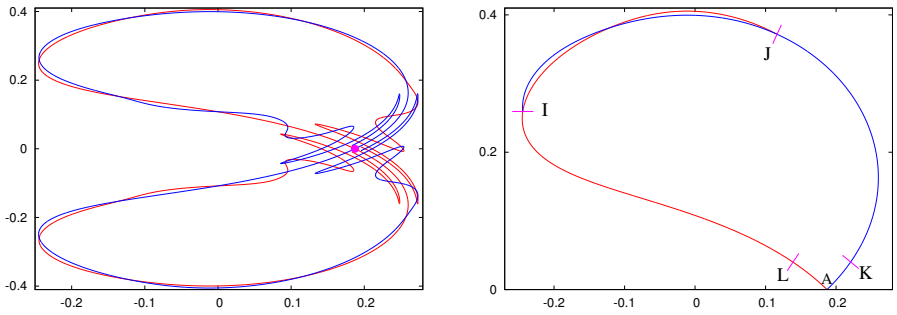

FIGURE 4. Invariant manifolds of the hyperbolic fixed point A on $p_x = 0$ for the Poincaré map $\mathcal{P}$ to be shown in Figure 5: W^u in red, W^s in blue. Left: A global view. Right: The upper part, showing a fundamental domain from I to J.

Here we assume that the behaviour of W^u wrt W^s is sinusoidal. This can be easily extended to more general cases, and the same happens if, instead of a symmetric case, one has different behaviour of the splitting in the upper and lower parts. See, e.g., [41] for derivation in a general context.

Except by some multiplicative constants, in the present example ζ coincides with the energy h and μ with the expression in (11). Similar expressions can be derived

in the heteroclinic case assuming, as it happens for (6), that the hyperbolic points are related by some symmetry.

Now we concentrate in the symmetric case and to points passing only through $\mathcal{D}_+$ (i.e., $\eta, \bar{\eta} > 0, s = 1$). Assume that η is close to some fixed value, η_0, and we write $\eta = \eta_0 + \Delta\eta, \bar{\eta} = \eta_0 + \overline{\Delta\eta}$ and

$$\log(\bar{\eta}) = \log(\eta_0) + \log(1 + \overline{\Delta\eta}/\eta_0) \approx \log(\eta_0) + \overline{\Delta\eta}/\eta_0,$$

keeping only linear terms in $\overline{\Delta\eta}$. This is a good approximation if $\overline{\Delta\eta}/\eta_0$ is small. In the $(\xi, \Delta\eta)$ variables the map becomes

$$\begin{pmatrix} \xi \\ \Delta\eta \end{pmatrix} \to \begin{pmatrix} \bar{\xi} = \xi + c_1 + b_1\overline{\Delta\eta} \\ \overline{\Delta\eta} = \Delta\eta + \mu\sin(\xi) \end{pmatrix},$$

where $c_1 = c - \log(\eta_0)/\zeta$, $b_1 = -1/(\eta_0 \times \zeta)$ and we do not write explicitly that ξ is taken mod 2π. Finally, define new variables $u = \xi, v = c_1 + b_1\Delta\eta$ and the map becomes

$$\begin{pmatrix} u \\ v \end{pmatrix} \to \begin{pmatrix} \bar{u} = u + \bar{v} \\ \bar{v} = v + \kappa\sin(u) \end{pmatrix}, \tag{14}$$

where $\kappa = b_1\mu$. The map (14) is the very popular standard map. It is well known that (14) has rotational invariant curves up to the so-called Greene's critical value $\kappa_G \approx 0.971635406$. For $\kappa < \kappa_G$, and not too close to the critical value, these invariant curves occupy most of the phase space. The dynamics is mostly chaotic for $\kappa > \kappa_G$ which implies $\eta_0 < \mu/(\kappa_G\zeta)$. See [43] for details and many examples and [42] for the case in which the upper and lower part of the separatrix map (or outer and inner parts) are different.

In the example (6) the small parameter is the energy h. Using an expression for μ as given in (11) and the fact that $\zeta = \mathcal{O}(h)$ justifies that the measure of the chaotic domain can be fitted by an expression like (8). The value of b_c is equal to $b_s - 1$, the values of a_c and a_s differ by a constant related to scaling and the values of c_c and c_s are identical.

4.2. **A variant of the Hénon-Heiles system.** An interesting variant of (6) is found when the $x^3/3$ is suppressed and we deal with

$$H_0(x, y, p_x, p_y) = \frac{1}{2}(x^2 + y^2 + p_x^2 + p_y^2) - xy^2. \tag{15}$$

Figure 5 shows the image of the Poincaré map, also for $y = 0, p_y > 0$ and on the level of energy $h = 0.1$. The levels of energy have a compact component until $h = 1/8$. The Poincaré plot shows 6 simple p.o., 4 of them elliptic and 2 hyperbolic, one of them at the boundary. The plot also displays the invariant manifolds of the hyperbolic p.o. located on $p_x = 0, x > 0$ that we shall denote as A. As for (6) there is a symmetry wrt $p_x = 0$. But, in contrast, the homoclinic points are not located in any symmetry line. Details on the manifolds were shown in Figure 4.

4.2.1. *Numerical results.* First we proceed to the computation of the fraction of regular points as in (7) using the methods as described. The results are shown in Figure 6. We also show, at the bottom part, a measure of the lack of coincidence of $W^u(A)$ and $W^s(A)$. In the present case one can not use some splitting angle as a measure. The reason is simple. If we consider an homoclinic point, as the one clearly seen in Figure 4, and do continuation wrt h, one can check that for some values of h the manifolds have a cubic tangency and new primary homoclinic points are created (or destroyed) in a fundamental domain. Details on the evolution will

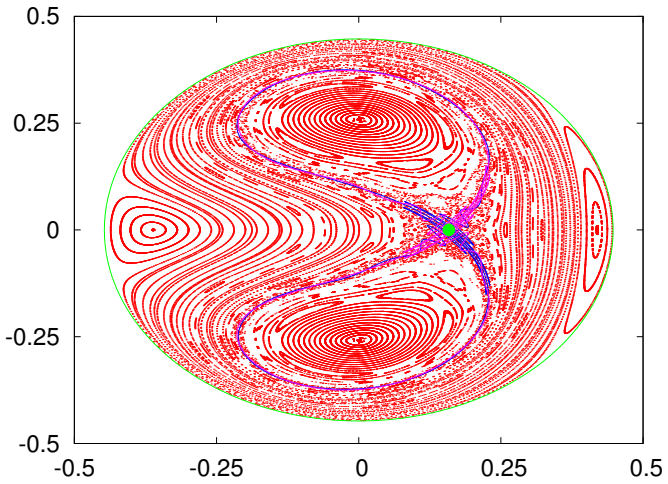

FIGURE 5. Poincaré map $\mathcal{P}$ related to (15) on the level $H^{-1}(0.1)$. The coordinates displayed are (x, p_x). See the text for details.

be shown in Figure 8 below. Hence, as a measure of the lack of coincidence of the manifolds we have used the sum of the absolute values of the areas of the lobes in a fundamental domain. We keep the name $\sigma(h)$ for that measure.

The first surprising thing is that, for values of h that can be already considered as small, the chaotic fraction is not tending to zero in a monotonous way. The second one is the similitude of the upper right plot and the lower one.

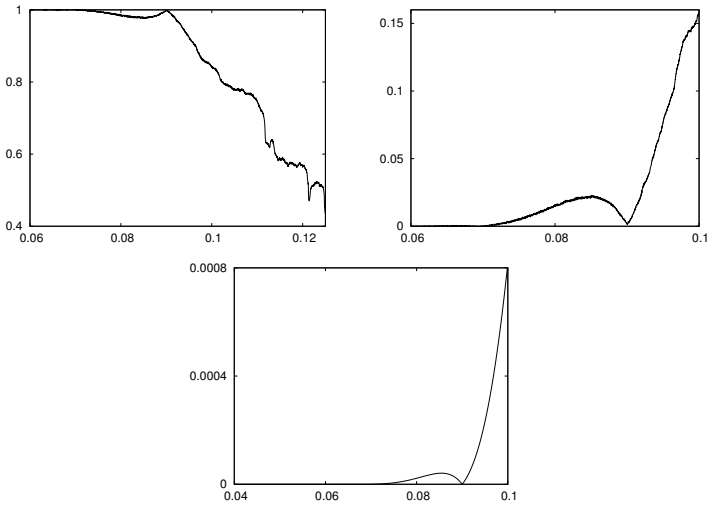

FIGURE 6. Top: On the left (resp. right) we show the regular (resp. chaotic) fraction $\psi(h)$ (resp. $1 - \psi(h)$) as a function of h. The bottom plot shows a measure of the lack of coincidence of the invariant manifolds, also as a function of h. See the text for details.

This suggests to go back to an splitting formula as (12). If the dominant part of the splitting has $\cos(2\pi\delta/\zeta(\varepsilon))$ as a factor, next harmonic will be relatively small (due to a prefactor containing $\exp(-4\pi\rho/\zeta(\varepsilon))$) and would explain the fact that the measures of the chaotic domain and of the lack of coincidence of the manifolds seem

to be zero when the cos term is zero. To check the suspected behaviour a fit has been done, of the log of both measures multiplied by h, but replacing a function like $\ell(h)$ in (8) by

$$\hat{\ell}(h) = ah + bh\log(h) - c + h\log(\cos(d/h + e)), \tag{16}$$

wrt the parameters a, b, c, d, e, where e should be seen as a phase. The results are shown in Figure 7.

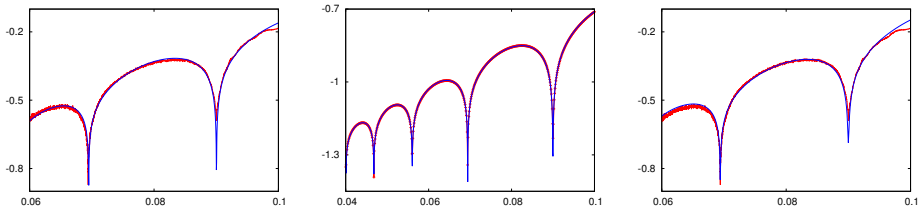

FIGURE 7. Left: Values of $h\log(1-\psi(h))$ for (15) and a fit (in blue) of the form (16) as a function of h. Middle: a similar plot using the measure σ instead of $1-\psi(h)$. Right: The values of $h\log(1-\psi(h))$ and a multiple of the fit for σ, changing only the values of a, b as done in Section 4.1. Compare with Figure 3.

To further illustrate the behaviour of the measure σ of the lack of coincidence of $W^u(A)$ and $W^s(a)$, we show in Figure 8 the evolution of the relative position of $W^u(A)$ wrt $W^s(a)$ around the minimum which can be seen in the middle part of Figure 7 near $h = 0.09$.

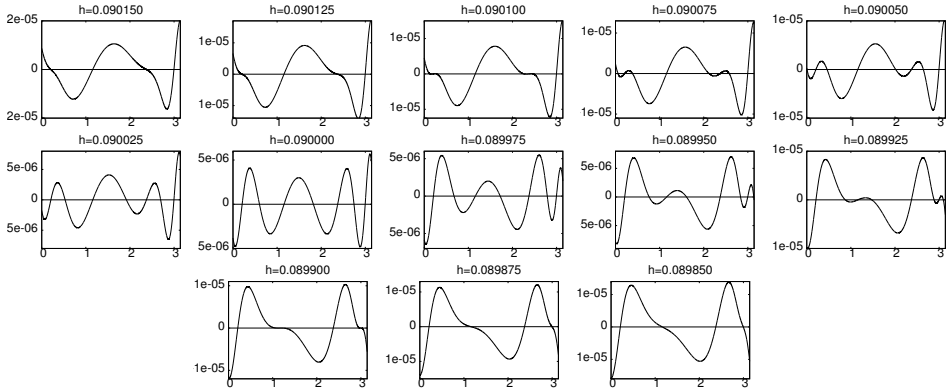

FIGURE 8. A movie of the position of W^u wrt W^s, as a function of h, around the rightmost minimum seen in Figure 7. It shows cubic tangencies and the creation/destruction of additional homoclinic points. We use $h \in [0.090150, 0.089850]$ with step 25×10^{-6}.

To compute the values of σ for this figure (and the two previous ones and next one) we use the following method. Many points are computed in $W^u(A)$ and $W^s(A)$ using a continuation parameter method with small stepsize, see [34], roughly on a range as seen in Figure 4 between the sections I and J. Then one looks at the computed points in polar coordinates from the elliptic point in $x = 0, p_x > 0$ that can be seen in Figure 5. Points in both manifolds, along the same radius and for equispaced arguments, are obtained from the previous data by local Lagrange

interpolation (using a suitable order to minimize the error). The difference of values of the radii allows to obtain plots as in Figure 8 and to estimate the value of σ.

4.2.2. *Theoretical support.* Around a value of h^* such that the dominant term in (12) becomes zero (we recall that h takes now the role of ε), compare also with (16), the contribution of the next harmonic is of the form

$$A_2\varepsilon^{B_2}\exp(-4\pi\rho/\zeta(\varepsilon))(\cos(4\pi\delta/\zeta(\varepsilon)+\varphi_2(\varepsilon))).$$

We can assume, generically, that it is different from zero and with negligible variations around h^*. Hence, the splitting function sf, which measures the position of $W^u(A)$ wrt $W^s(A)$ in a fundamental domain, can be written as

$$sf(\xi,\Delta H)=\gamma(\Delta\sin(\xi)+\sin(2\xi)), \tag{17}$$

where Δ is a multiple of $h-h^*$ and ξ is an angular variable ranging in $[0,2\pi]$ when the points in the manifolds move in a fundamental domain. The function sf in (17) has a triple zero at π for $\Delta=2$ and at 0 for $\Delta=-2$, values which can be identified with the results for $h\approx 0.0901$ and $h\approx 0.0899$ in Figure 8. Note that the horizontal variable in Figure 8 is not the angle ξ in (17), but the auxiliary angle introduced when taking polar coordinates for the computation of σ, as described before.

Using an expression for sf as in (17) the value of σ is easily computed to be $4+\Delta^2$ for $|\Delta|\le 2$ and $4|\Delta|$ for $|\Delta|\ge 2$. The Figure 9 shows the results near the two rightmost minima seen in the middle plot in Figure 7, showing a perfect agreement with the theoretical behaviour. In the left plot the behaviour of $\sigma(h)$ around the rightmost most minimum in the middle plot in Figure 7 is shown in the range $[0.0898, 0.0902]$ with step 10^{-6}. The blue points correspond to the h for which triple zeros occur. In the right one a similar plot for next minimum, for $h\in[0.069415, 0.069418]$ with step 10^{-8}. The minimum is found for $h\approx 0.06941635$. For simplicity we display $h-0.0694165$, the blue points have the same meaning as above and a fit with the theoretical prediction coincides with the results within the present resolution.

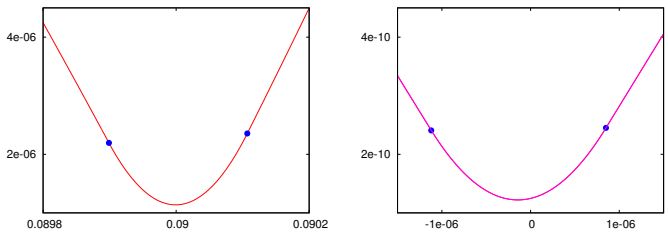

FIGURE 9. The behaviour of $\sigma(h)$ around the two rightmost minima in the middle plot in Figure 7. See the text for details.

In Section 4.1.2 we discussed the role of the separatrix map and, later, the standard map (14), in bounding regions which contain most of the chaotic dynamics. From Greene's value κ_G we related the size of the splitting with the measure of the chaotic domain. We can question the changes to be introduced using (17) instead of $\kappa\sin(\xi)$ in (14). This replacement leads to one of the many generalizations of (14). To check the effect we study a normalized version of the form

$$\begin{pmatrix} u \\ v \end{pmatrix} \to \begin{pmatrix} \bar u = u+\bar v \\ \bar v = v+\kappa(\cos(2\pi\psi)\sin(u)+\sin(2\pi\psi)\sin(2u)) \end{pmatrix}, \tag{18}$$

where $\psi \in [0, 1/4]$ is a parameter of the family. In this way we expect, given ψ, to find a critical value $\kappa(\psi)$ such that at this value (18) has all the rotational invariant curves destroyed. Obviously $\kappa(0) = \kappa_G$ and a scaling shows $\kappa(1/4) = \kappa_G/2$. However the behaviour is a little bit more complicated. Figure 10 shows the couples (ψ, κ) for which (18) has rotational invariant curves. Outside the gray domain they are all destroyed. Note that for some ψ we can recover invariant curves by increasing κ. But these details do not change, except by a multiplicative factor, the estimates of the measure of the chaotic domain.

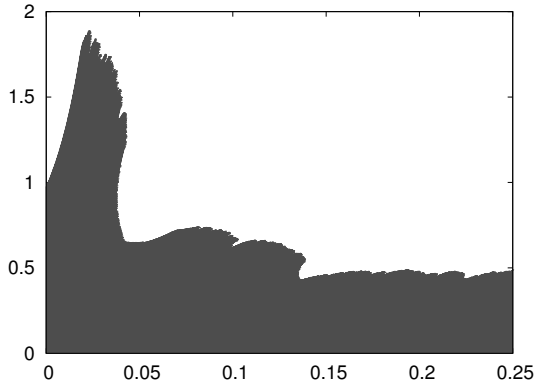

FIGURE 10. Domain of existence of rotational invariant curves for (18) where the horizontal (resp. vertical) variable corresponds to ψ (resp. κ).

4.3. **A non-resonant 2 dof Hamiltonian.** After the two resonant cases in previous sections it can be interesting to look at a non-resonant case. An elementary example is obtained by a minor change in (15)

$$H_{nr}(x, y, p_x, p_y) = \frac{1}{2}(x^2 + y^2 + p_x^2 + 2p_y^2) + xy^2, \tag{19}$$

with frequencies $1, \sqrt{2}$ at the origin and with energy levels having a compact component until $h = 1/8$. According to Lyapunov theorem, there are only two simple p.o. for small h: one on $y = p_y = 0$, as before, and the other with one point on $p_x = 0, x < 0$ on the Poincaré section $y = 0, p_y > 0$. Both p.o. are elliptic.

Before showing the results on the fraction of chaotic dynamics it is instructive so show a plot on the evolution of the rotation number ρ as a function of the energy and the initial condition, taking this condition on the Poincaré section with $p_x = 0$. As done in (9) we can scale variables by a factor ν: $x = \nu X$, etc, which amounts to putting ν in front of the cubic terms in (15). Taking $\nu^2 = 2h$ implies that the boundary of the Poincaré section is $X^2 + P_X^2 = 1$.

The results are shown in Figure 11 using (X, h) as variables. The red curve starting at $(0, 0)$ shows the location X_{po} of the p.o. The initial conditions are taken in $X \in (X_{po}, 1)$. Except for extremely tiny domains the points in white correspond to $\rho \notin \mathbb{Q}$. The curves in black correspond to extrema of ρ. For small h the value of ρ, that we can denote as $\rho_h(X)$, is decreasing. The maximum located in the p.o. becomes a minimum at $h \approx 0.03$ and a curve of maxima of $\rho_h(X)$ wrt X emerges. We denote it as nt_1, to stress that around it a non-twist behaviour appears, see Section 2.2. Another non-twist curve, corresponding to minima of $\rho_h(X)$, shows up from the boundary $X = 1$ at $h \approx 0.0534$ and will be denoted as nt_2.

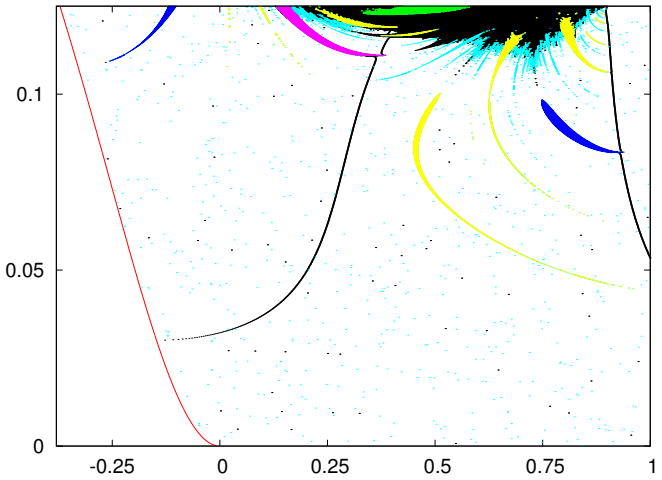

FIGURE 11. Information obtained from the rotation number as a function of position and energy. The lines show location of p.o. and places where the twist condition fails. The wedges correspond to islands and the black domains to chaos. See text for details.

Periodic orbits, the elliptic ones giving rise to stability islands, emerge from the simple p.o. or from $nt_{1,2}$. The blue and magenta domains correspond to p.o. with $\rho = 1/4$ and $\rho = 2/7$, respectively. The yellow domains to p.o. with periods between 9 and 19, mainly dominated by the p.o. with $\rho = 3/11, 3/13, 5/19$ and $3/10$. Higher order p.o. are marked in light blue. The green and black domains correspond to period 3 and chaos, respectively.

4.3.1. *Numerical results.* In Figure 12 we display the results concerning the fraction $1 - \psi(h)$ of points with chaotic dynamics. It becomes extremely small for $h < 0.1$, not detectable unless one uses an enormous amount of points with the methods of Section 3. Some tiny domains appear near $h = 0.0834$ but the detected chaotic fraction is, at most, 0.002 and disappears by increasing h.

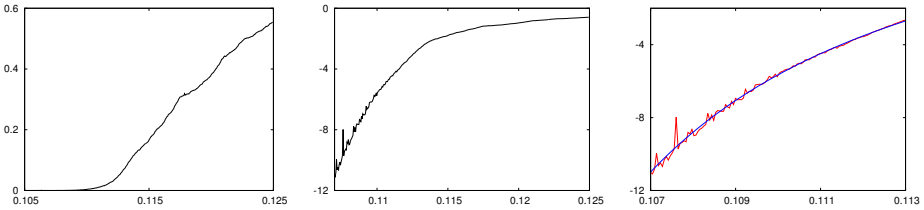

FIGURE 12. Results concerning the chaotic fraction for (19). Left: the values of $1 - \psi(h)$ vs h. Middle: Same plot using log scale for $1 - \psi(h)$. Right: A part of previous plot and an adapted fit. See the text.

The reason of this fact is easy to understand at the light of Figure 11. It turns out that the minimum value of ρ which occurs at the nt_2 curve reaches the value $\rho = 1/4$. Then the right blue domain in Figure 11 is born, but initially there are some meandering curves (see the end of Section 2.2) and the related hyperbolic p.o. give a little amount of chaos. This phenomenon was found to occur also in Hill's

problem [38]. Increasing h the interaction between the p.o. of period 4 disappears and most of the chaos is gone.

On the other hand, in the right part of Figure 12 a fit is shown in a selected range, starting when chaos becomes visible on the left plot. Some little peaks are mainly due to the effect of chaotic zones associated to hyperbolic p.o. with $\rho = 3/11$ and $\rho = 3/13$ and the possible effect of the sampling. But the main effect in the displayed range is due to the fact that the elliptic p.o. of period 4, mentioned in the above paragraph, becomes hyperbolic. This corresponds to the end of the right blue domain in Figure 11.

To check this behaviour a fit of the data in Figure 12 right has been done using a function of the form

$$\log(1 - \psi(h)) = a + b \log(h - h_c) - \frac{c}{(h - h_c)^d}, \tag{20}$$

where we consider as parameters to fit not only a, b, c but also h_c and the exponent d. The best fit has been found for $h_c = 0.09850650$ with $d = 1$. But the value h_c coincides with the passage of the 4-periodic orbits from elliptic to hyperbolic. This shows that the main contribution to the chaos is an exponentially small effect related to the main hyperbolic p.o.

4.3.2. *Theoretical support.* Beyond the facts and explanations just presented we want to discuss why so small amount of chaos is detected even for relatively large values of the energy h.

The basic idea is that being the source of chaos the existence of splitting of the manifolds of hyperbolic p.o., one should look when they appear. If the frequencies ω_1, ω_2 at the origin satisfy a Diophantine condition (3), as in (19), a given resonance appears at some distance from the origin.

Given a Hamiltonian H around a fixed point, one of the basic tools to try to have a nearby integrable system are the normal forms. If $H = H(\varphi, I)$ in angle-action variables, one can try to get rid of the dependence wrt φ by means of a sequence of transformations. If the frequencies at $I = 0$ satisfy the non-resonant condition

$$(k, \omega(0)) \neq 0 \quad \text{for all} \quad k \in \mathbb{Z}^n \setminus \{0\}, \tag{21}$$

this is always formally possible for all N. The changes of variable to cancel, successively, the terms which are not depending only on the I_j coordinates, can be easily obtained as the time-1 flow of auxiliary Hamiltonian systems, these changes being then canonical (and close to the identity). It is clear that the domain of analyticity of the current Hamiltonian after every change can have successive reductions [12].

In all the above cases one can write the transformed Hamiltonian as

$$\mathcal{H} = NF_N + \mathcal{R}_{>N}, \tag{22}$$

where NF_N stands for the normal form truncated to order N included (in the Cartesian coordinates, order $N/2$ in I) and which is integrable, and $\mathcal{R}_{>N}$ denotes the remainder and which can be considered as a perturbation of NF_N to apply KAM results in a small vicinity of the fixed point if $\mathrm{Hess}(NF_N(0))$ is regular. There are also results for the singular case when some non-degeneracy condition appears at higher order.

For our purpose it is enough to consider NF_4 and we restrict, for the moment, to $n = 2$ dof. Then $\omega(I) = \omega(0) + AI + \mathcal{O}(|I|^2)$, where AI is the linear part coming from the terms of degree two in I in NF_4. To have a resonance $(k, \omega(I)) = 0$ for

some $k \in \mathbb{Z}^2 \setminus \{0\}$, using (3) for $\omega(0)$ and the fact that $|I| = \mathcal{O}(h)$, it is found that if the order k is $|k|_1$ the energy should satisfy

$$h > \hat{c}/|k|_1^{1+\tau}, \tag{23}$$

where τ is the exponent in (3) for $\omega(0)$ and $\hat{c}$ depends also on the Diophantine condition and on the norm of A. Reciprocally, given h, small, the minimal order of a harmonic (k, φ) giving rise to a resonance is of the form $|k|_1 = \mathcal{O}(h^{-1/(1+\tau)})$. These harmonics appear in the remainder $\mathcal{R}_{>4}$ and have bounds of the form $\exp(-\rho|k|_1)$, where now ρ stands for the width of the analyticity domain of $\mathcal{H}$ wrt φ.

Summarizing: The amplitude of the resonant harmonics is exponentially small in the energy and, furthermore, the measure of the chaotic domain they create is exponentially small with respect to the distance to the creation of the hyperbolic p.o. A type of bounds similar to the ones derived in [28] for KAM tori.

4.4. **A family of resonant 3 dof Hamiltonian systems.** Now we pass to 3 dof. The following family of Hamiltonian systems is considered

$$H(x, y, z, p_x, p_y, p_z) = \frac{1}{2}(x^2 + y^2 + z^2 + p_x^2 + p_y^2 + p_z^2) + Ax^2y + By^2z + Cz^2x, \tag{24}$$

with $A^2 + B^2 + C^2 > 0$. It is not restrictive to assume $A, B, C \geq 0$ and, clearly, we can normalize the coefficients to satisfy $A + B + C = 3$. It can be seen as a generalization of (6) to 3 dof; it allows to study the 1:1:1 resonance, and it also allows to break all symmetries if $A < B < C$. It contains symmetric and limit cases. The levels of energy have a compact component, in all cases, provided $0 < h \leq h_m(A, B, C)$, where the critical value $h_m(A, B, C)$ is minimum (1/72) for $A = B = 0$ and maximum (1/18) for $A = B = C$.

As a preliminary step we can check for integrability. One possibility is to look for rectilinear solutions, that is, for solutions such that $x = \beta_1\varphi(t), y = \beta_2\varphi(t), z = \beta_3\varphi(t)$, with $\beta_1, \beta_2, \beta_3 \in \mathbb{C}$. For every set of values of (A, B, C) there exist several such solutions. In the case of (24) the equation for φ has elliptic functions as solutions. Another possibility is to implement the general methodology given in [20], select two closed paths, γ_1, γ_2 in the Riemann surface Γ and check for the monodromy along $\gamma_2^{-1} \circ \gamma_1^{-1} \circ \gamma_2 \circ \gamma_1$. Any of the two methods shows that (24) is non-integrable for all (A, B, C). We remark that, for some symmetric cases, it can be necessary to check different rectilinear solutions. Some of the solutions can give no obstructions to integrability using VE1.

A problem which appears immediately is the following: The terms in a normal form are in involution with the quadratic part H_2. In the 1:1:1 resonance, as it happens in the 1:1 case, a normal form NF can be computed to any order, including resonant terms which are of even degree in (q, p). With 2 dof the NF truncated to any order, as approximation to the full Hamiltonian, is an integrable system (NF and H_2 being the two first integrals, except in the extremely degenerate case in which NF is a function of H_2). This is no longer true with 3 dof. Hence, we should face a non-integrable normal form.

Another way to realize this is that a Poincaré map in the 3 dof case is close to the identify because of the 1:1:1 resonance. The 4D symplectic map obtained in any level $H^{-1}(h)$ can be approximated by the time-1 map of a slow Hamiltonian with 2 dof, but this one is non-integrable in general. As a conclusion, we can expect that the chaotic fraction tends to a positive limit when $h \to 0$.

But, at the same time, the maximal Lyapunov exponents are $\mathcal{O}(h)$, which can require a long integration time to decide about being positive or zero. This problem has an easy solution, looking for the behaviour of a limit Hamiltonian. We describe the steps:

1) First we scale variables as in (9) in the 3 dof and divide H by ν^2.
2) A normal form is computed and the Hamiltonian has the form $H_2 + \nu^2 H_4 + \nu^4 H_6 + \ldots$, where H_k denote homogeneous terms of degree k. It is clear that the $H_4, H_6, \ldots$ parts contain resonant terms.
3) Passing to angle-action variables (φ, I) the term H_2 becomes $H_2 = I_1 + I_2 + I_3$. From this it follows $\dot{\varphi}_j = 1 + \mathcal{O}(\nu^2), j = 1, 2, 3$. As usual, this suggest to introduce new variables $\bar{\varphi}_j = \varphi_j - t$. The equations obtained for $\dot{\bar{\varphi}}_j, \dot{I}_j$ contain the factor ν^2 and are 2π-periodic in t.
4) Then we apply averaging wrt t. This produces an slow autonomous system which has ν^2 as factor. Scaling time by ν^2 the factor cancels and the system has the form $H_4(\bar{\varphi}, I) + \nu^2 H_6(\bar{\varphi}, I) + \ldots$. Taking the limit $\nu \to 0$ only H_4 remains.
5) We note that, because of the resonant part of the NF, H_4 can contain terms in which some of the factors $I_1^{1/2}, I_2^{1/2}, I_3^{1/2}$ appear. This is not convenient for the numerical integration. Hence, we return to Cartesian coordinates, to be denoted as (u, v, w), and the corresponding momenta. Note that, after the scaling and passage to the limit, one has that $I_1 + I_2 + I_3$ is constant. But this is only used as a check.

The limit Hamiltonian, homogeneous of degree 4, is found to be

$$\begin{aligned}
&4H_4(u,v,w,p_u,p_v,p_w) = \\
&\quad A^2(-5u^4+(-20v^2-10p_u^2+4p_v^2)u^2-48uvp_up_v-5p_u^4+(4v^2-20p_v^2)p_u^2) \\
&+B^2(-5v^4+(-20w^2-10p_v^2+4p_w^2)v^2-48vwp_vp_w-5p_v^4+(4w^2-20p_w^2)p_v^2) \\
&+C^2(-5w^4+(-20u^2-10p_w^2+4p_u^2)w^2-48wup_wp_u-5p_w^4+(4u^2-20p_u^2)p_w^2) \\
&+AB((-20vw-28p_vp_w)u^2+8(vp_w+wp_v)up_u+(-28vw-20p_vp_w)p_u^2) \\
&+BC((-20wu-28p_wp_u)v^2+8(wp_u+up_w)vp_v+(-28wu-20p_wp_u)p_v^2) \\
&+CA((-20uv-28p_up_v)w^2+8(up_v+vp_u)wp_w+(-28uv-20p_up_v)p_w^2).
\end{aligned} \tag{25}$$

Note that, due to the scaling and passage to the limit, the level of H_4 is irrelevant.

4.4.1. *Numerical results.* To estimate the value of the limit integrable fraction $\psi(0) = \lim_{h\to 0} \psi(h)$, depending on A, B, C, we proceed as described in Section 3 but, as announced in 3.3, using the formulation in (25). The Figure 13 shows the result. As expected, the values of $\psi(0)$ are away from 1 for most of the values of the parameters, except for the cases $(0, 0, 3)$ and $(1, 1, 1)$, to be discussed in Section 4.4.2.

The behaviour of $\psi(h)$, proceeding directly with (24), has been checked for several values of (A, B, C). In Figure 14 we illustrate the results with a small sample of cases, for values of (A, B, C) equal, from left to right, to $(0, 1, 2), (1/2, 1, 3/2)$ and $(0, 3/2, 3/2)$. In Figure 15 we display the behaviour of the estimates $\psi(h)$ for $h = 10^{-4}$ as a function of the maximal time t_m used to estimate whether the dynamics is regular or chaotic. The values for $t_m \approx 10^8$, from top to bottom, correspond to the cases of Figure 14 from left to right. It is clear that using, e.g., $t_m = 10^6$ can produce wrong estimates. The size of the samples used in these computations exceed 10^5 initial points, going up to a value close to 10^6 in critical cases.

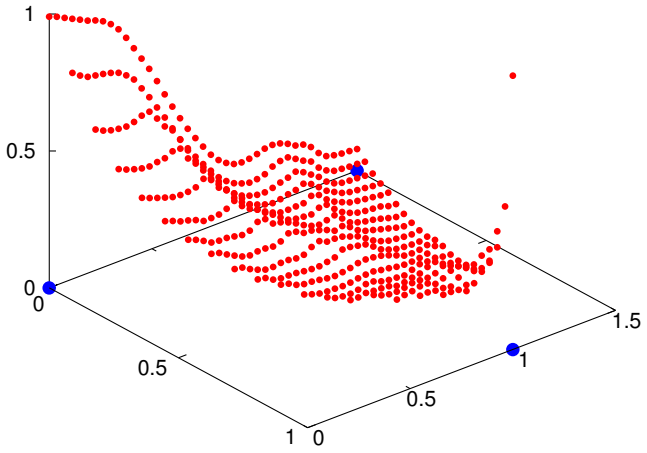

FIGURE 13. The limit fraction of integrability $\psi(0)$ as a function of $A \le B \le C$. The horizontal variables are A, B and $C = 3-A-B$.

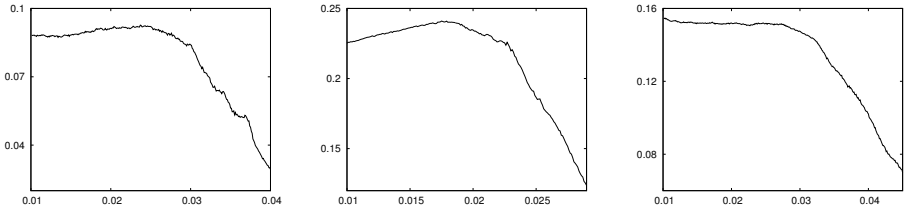

FIGURE 14. Behaviour of $\psi(h)$ using directly (24). From left to right the values used for (A, B, C) are $(0, 1, 2), (1/2, 1, 3/2)$ and $(0, 3/2, 3/2)$.

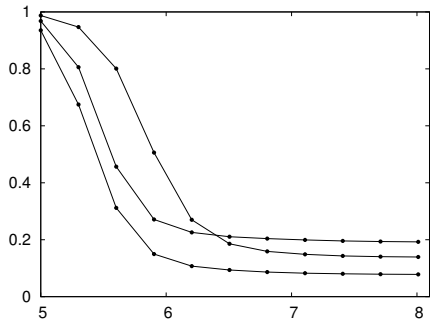

FIGURE 15. Behaviour of the estimates of $\psi(h)$ for $h = 10^{-4}$ as a function of the maximal time t_m used in the computations, shown in $\log_{10}$ scale. The estimated limit values are 0.192, 0.139 and 0.078, approximately. See the text for details.

4.4.2. *Theoretical support.* It has already been explained why $\psi(0)$ is different from zero for most of the (A, B, C) values, due to the lack of integrability of the normal form at order 4. It remains to explain the exceptional cases. The case $(0, 0, 3)$ decouples as two independent Hamiltonian systems $H^{(1)} = \frac{1}{2}(y^2 + p_y^2)$ and $H^{(2)}(x, z, p_x, p_z) = \frac{1}{2}(x^2 + z^2 + p_x^2 + p_z^2) + 3z^2x$. Hence, the dynamics is the product of an harmonic oscillator times the system considered in (15) (the effect of the

scaling parameter is irrelevant). Hence, $1-\psi(h)$ tends exponentially to zero when $h \to 0$. This fact is not detected by (25), which is able to detect chaos $\mathcal{O}(h)$ and, therefore, it gives $\psi(0) = 1$.

In the case $A = B = C$, due to the symmetry, one has that the variable $u = x + y + z$ is leaded by the 1 dof Hamiltonian $H^{(1)}(u, p_u) = (u^2 + p_u^2)/2 + u^3/3$. Hence, the system (and also the normal form) has an extra integral. The behaviour is similar to the 1:1 case. As before, (25) is not able to detect the exponentially small lack of integrability. The Figure 16 shows the values of $1-\psi$ in that case. They are very small even for h close to the limit value $1/18$.

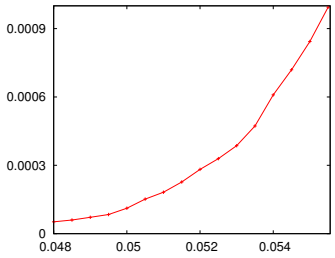

FIGURE 16. Values of $1-\psi(h)$ vs h for the case $A = B = C$.

As it can be expected the case $A = B = C$ has a strong similitude with a resonant Hamiltonian with 2 dof. In the Poincaré section Σ defined by $x = 0, p_x > 0$ there are three fixed points $P_j, j = 1, 2, 3$ of the Poincaré map $\mathcal{P}$. They are of centre×saddle type. The invariant manifolds $W^{u,s}(P_j), j = 1, 2, 3$ also lie on Σ. Figure 17 shows these fixed points, their invariant manifolds and some details, projected on the $(z, \dot{y})$ variables. The level of energy is $h = 0.333^2/2$, very close to the limit $1/18$. We see that the plots are reminiscent of the resonant 2 dof case.

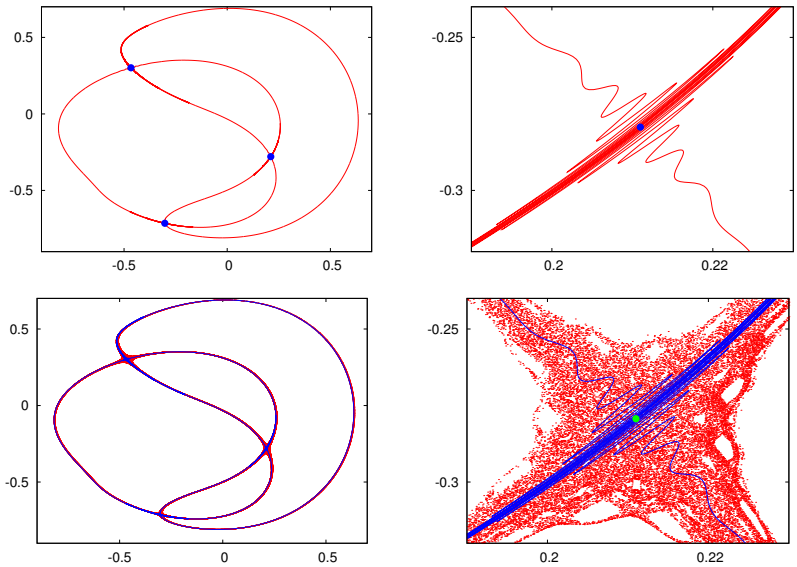

FIGURE 17. The three fixed points of the map $\mathcal{P}$ on Σ, projected on $(z, \dot{y})$. Top left: The fixed points and the unstable manifolds (in red). Top right: A magnification close to one of the fixed points. The bottom plots are similar, but they include the orbit of a nearby initial point (in red) and the manifolds are plotted in blue.

As the fixed points of $\mathcal{P}$ are of centre×saddle type, they have 2D centre manifolds $W^c(P_j), j = 1, 2, 3$. They are a particular, but relevant, case of normally hyperbolic invariant manifolds (NHIM). On these manifolds KAM theorem generically applies and there are invariant circles. They have unstable and stable manifolds that, generically, do not coincide, see [11] for typical examples near a double resonance in 4D symplectic maps and [6] for estimates of the splitting.

On can take an initial point close to one of the invariant circles $\mathcal{C}_j$ in $W^c(P_j)$ for some j and look at the successive Poincaré iterates on Σ. We expect that the points will move close to $W^u(\mathcal{C}_j)$ and return to a vicinity of the same circle or of some other circle, either nearby (in the same $W^c(P_j)$) or in another centre manifold $W^c(P_k), k \neq j$.

This is what is observed in Figure 18. It gives evidence of the homoclinic and heteroclinic connections between the three centre manifolds $W^c(P_j), j = 1, 2, 3$. But despite the large number of iterates done (10^9, showing one point every 5000 iterates) the chaos looks confined in very narrow domains. This has to be expected because there is no possibility of diffusion due to the existence of the additional integral $H^{(1)}(u, p_u)$. The same behaviour is observed for many other initial points close to some of the invariant curves in one of the centre manifolds. This is in strong contrast with the example to be presented in Section 4.6.

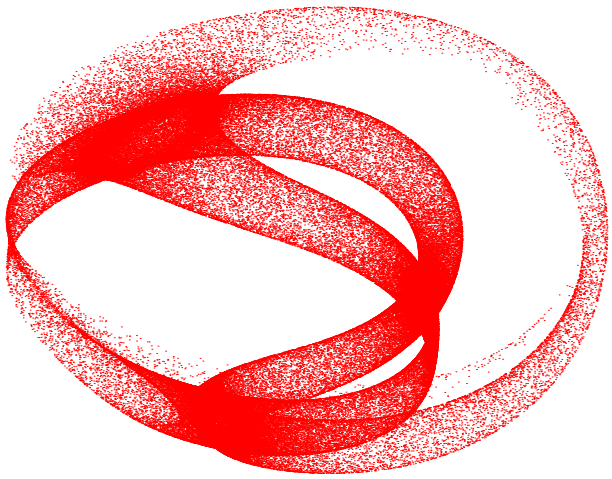

FIGURE 18. Iterates of an initial point close to one of the centre manifolds around one of the three fixed points of $\mathcal{P}$ in Σ. The points in Σ are projected on the variables $(y, z, \dot{y})$ and a 3D view is shown. See the text for details.

To have further evidence of the lack of diffusive properties for the case $A = B = C$ we have proceeded as follows. One can take a vertical slice in Figure 18. This means: select a value y_0 of y and keep only the iterates which fall within a distance of y_0 less than some small value η. This is an approximation of a 3D section of the 4D Poincaré section. If the diffusion is irrelevant we expect to have points in circles, as it would be the case if the invariant circles $\mathcal{C}_j$ in the $W^c(P_j)$ would have separatrices connecting them.

We should expect 6 sets of points close to circles, corresponding to the two connections from $\mathcal{C}_j$ to $\mathcal{C}_k$ where $k \neq j, j, k \in \{1, 2, 3\}$. Suitable choices for y_0 and

η are $y_0 = 0, \eta = 2.5 \times 10^{-5}$. This has been done starting near several invariant circles in $W^c(P_1)$, at different distances from P_1. Even doing 10^9 Poincaré iterates, the number of points falling in the slices ranges from 19,000 to 25,000, depending on the distance from the curve to P_1. The results are shown in a 3D view in Figure 19 for a choice of three sets of data, using a small, intermediate or larger distance to P_1. Note that one of the sets of points appears broken. This is due to the fact that Σ is not a global transversal section.

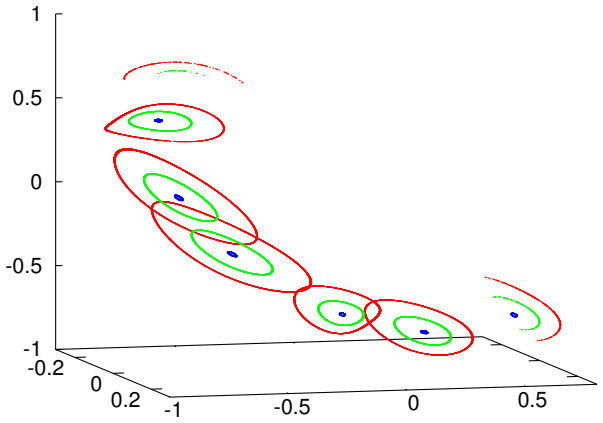

FIGURE 19. Slices of three cases like the one in Figure 18 using $|y| < 2.5 \times 10^{-5}$ and considering the full set of 10^9 iterates. The variables displayed are $(z, \dot{y}, \dot{z})$ in the domain $[-0.3, 0.3] \times [-1, .8] \times [-1, 1]$. See the text for additional information.

4.5. **A simple non-resonant 3 dof Hamiltonian system.** As a last example in that series we consider a non-resonant Hamiltonian, obtained from (24) with $A = B = C = 1$ by simple changes in the coefficients of the momenta

$$H(x, y, z, p_x, p_y, p_z) = \frac{1}{2}(x^2 + y^2 + z^2 + p_x^2 + 2p_y^2 + 3p_z^2) + x^2 y + y^2 z + z^2 x, \quad (26)$$

with frequencies $1, \sqrt{2}, \sqrt{3}$ at the origin. The energy is also restricted to $h \leq 1/18$ to have a compact level.

4.5.1. *Numerical results.* Figure 20 shows the values of $1 - \psi(h)$ as a function of h. The values go quickly to zero as h decreases, as happened in Section 4.3. In the right plot we also display a fit to the numerical data. But in contrast to the 2 dof case now the fitting function used for $\log(1 - \psi(h))$ is not like the one used in (20), but of the form

$$\log(1 - \psi(h)) = a + b \log(h - h_c). \quad (27)$$

The exponentially small term is missing. The best fit has been found for $h_c = 0.01656$. The reasons for that change in the local behaviour of the chaotic fraction will be given in 4.5.2.

For $h = 0.035$ the chaotic fraction is ≈ 0.063. Figure 21 shows the location of the chaotic zones for a simple set of initial data. One can distinguish different diffusive channels, associated to simple resonances, that is, places where there are 2D tori whose frequencies satisfy $(k, \omega) = 0$ for some $k \in \mathbb{Z}^3 \setminus \{0\}$. But one can

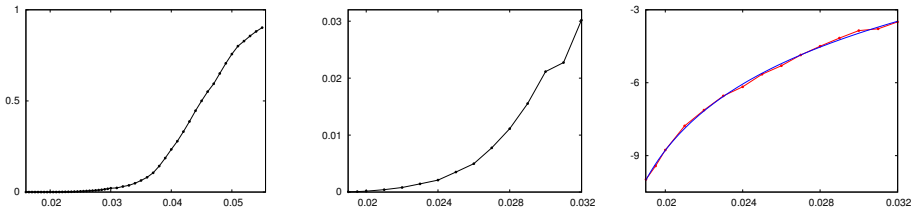

FIGURE 20. Left: Values of $1-\psi(h)$ as a function of h. Middle: A magnification on the interval $[0.019, 0.032]$. Right: On the same interval the values of $1-\psi(h)$ are shown in log scale and a fit. See the text and Section 4.5.2.

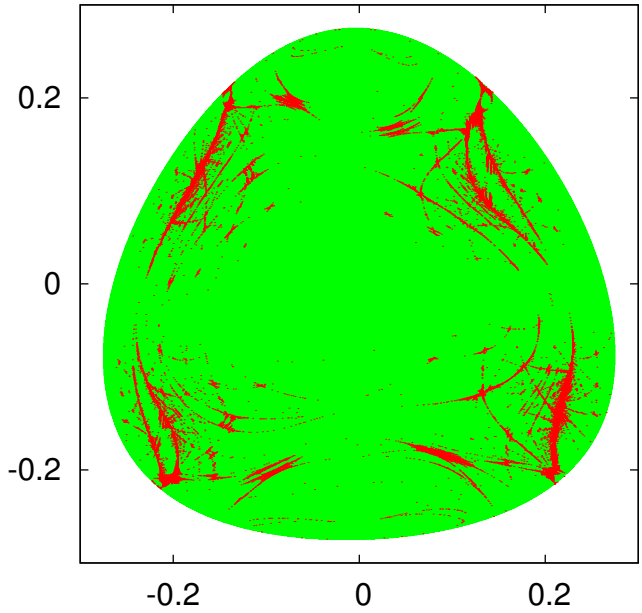

FIGURE 21. Location of the chaotic zones (in red) starting at a point of coordinates (x, y) with $p_x = p_y = p_z = 0$ and $z > 0$ derived from (26) for the energy level $h = 0.035$.

also see places where these channels meet, associated to double resonances, where $(k, \omega) = 0$ holds for two independent vectors $k^{(1)}$ and $k^{(2)}$. This is equivalent to the condition $\omega_1(I)/p = \omega_2(I)/q = \omega_3(I)/r$ for some integers p, q, r. If the level of energy is reduced to $h = 0.025$ the chaotic fraction decreases to ≈ 0.0035 and only a few spots of chaos are seen in Figure 22.

By looking at the middle of the red spot near $x = -0.0916, y = -0.1864$ in Figure 22, it is easy to find a periodic orbit. A 3D view is shown in Figure 23. It is clearly seen that it has two points with zero velocity. Other similar orbits emerge from the other red spots.

For this p.o. each one of the x, y, z variables oscillates in a close to sinusoidal way. The number of oscillations in one period, $T \approx 122.461344$, is 19, 27 and 33, respectively. The ratios 27/19 and 33/19 are rather close (differences below 0.007) to $\sqrt{2}$ and $\sqrt{3}$, respectively. The orbit has an elliptic-hyperbolic character and, therefore, there exists an associated 2D centre manifold on a Poincaré section.

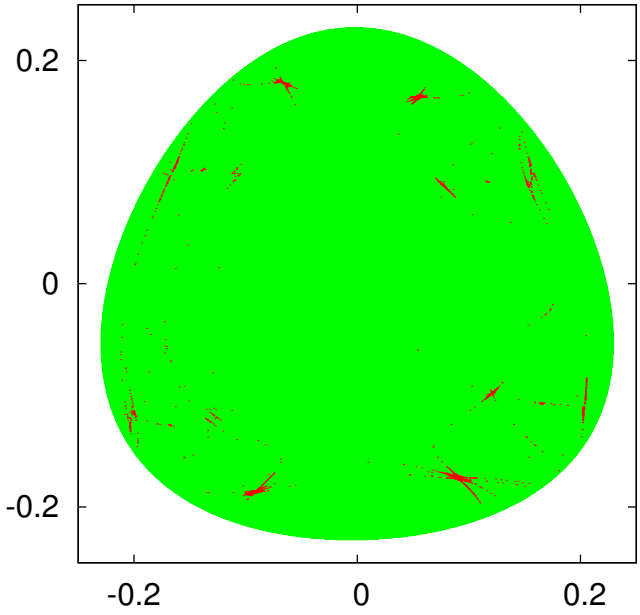

FIGURE 22. Similar to Figure 21 on $h = 0.025$.

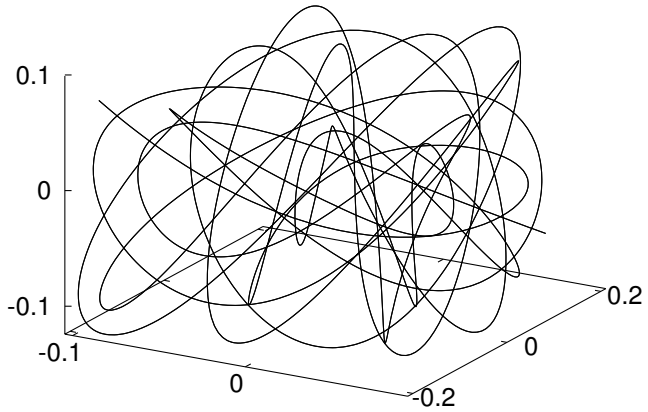

FIGURE 23. A periodic orbit of (26) in the middle of one of the red spots in Figure 22. See the text for details.

4.5.2. *Theoretical support.* First of all, as we did in Section 4.3, we can look for the distance to the origin to have a given resonance, either simple of double. Assume that the frequencies $\omega(0)$ at the origin are $1, \omega_2, \omega_3$. It is not restrictive to assume $\omega_1 = 1$ because this can always be achieved by scaling time. For the simple resonance we assume $\omega(0)$ satisfies (3). We shall use τ_1 instead of τ, to stress that it refers to simple resonance. Proceeding as in Section 4.3.2 it is found a condition like (23) for the energy to have a resonance of order $|k|_1$.

To measure the distance to double resonance one can use the simultaneous Diophantine approximation and look, in our present case, for

$$\delta_m(\omega_2, \omega_3) = \min_{p \le m} \{ \min_{(q_2, q_3) \in \mathbb{Z}^2} |(q_2 - p\omega_2, q_3 - p\omega_3)|_\infty \}, \tag{28}$$

where a Diophantine condition is written now as $\delta_m(\omega_2, \omega_3) \geq c/m^{\tau_2}$. As in the case of the simple resonance it is easy to obtain that to have a simultaneous approximation of order m requires $h > \tilde{c}/m^{1+\tau_2}$. Again, as in Section 4.3.2, the harmonics $q_2\varphi_1 - p\varphi_2$ and $q_3\varphi_1 - p\varphi_3$ have amplitudes which satisfy bounds of the form $< \exp(-c^* h^{-1/(1+\tau_2)})$ for some $c^* > 0$.

This leads, either in the case of simple or double resonance, to exponentially small bounds of the chaotic domains as a function of h.

As an example, and using the frequencies $(1, \sqrt{2}, \sqrt{3})$ the Figure 24 shows, for increasing values of $|k|_1$ and m, respectively, the places at which the bounds in (3) and in (28) decrease. The vertical variable represents the linear combination in (3) or the minimum in (28). Both variables are represented in $\log_{10}$ scale. The blue lines represent linear fits. The slopes found are $\tau_1 \approx -2.035$ for the simple resonance (lower data) and $\tau_2 \approx -1.524$ for the double resonance (upper data).

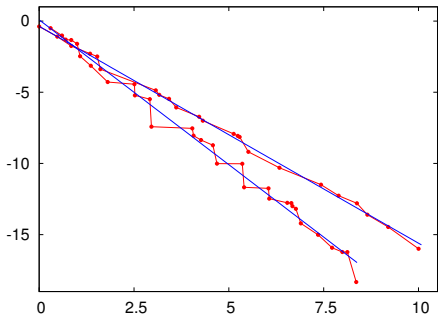

FIGURE 24. Values of $|k|_1$ and m, for simple and double resonance, at which the Diophantine bounds decrease, using the frequencies of (26) at the origin and fits of the decreasing rate. Variables represented in $\log_{10}$ scales. See the text for details.

When in a 4D symplectic map a resonance shows up, either simple or double, starting at a critical value of the energy $h = h_c$ it creates a NHIM. We can think of the vicinity of an elliptic-hyperbolic fixed point or the product of a cylinder times a pendulum-like map. These are the typical models. In both cases, either in the centre manifold of the fixed point or in the cylinder, one finds, generically, a Cantor set of invariant curves, with relative large measure. The size of the NHIM will change as a function of $h - h_c$ and one can expect that it behaves as a power of $h - h_c$. Despite the splitting of the manifolds of the invariant curves is exponentially small under reasonable conditions, see [6], the measure of the chaotic domain behaves as the size of the NHIM if there is no additional restriction, against what was found in Section 4.4 for $A = B = C$.

This explains why the fit of the form used in (27) gives good results in Section 4.5.1.

4.6. **Motion in the 3D RTBP evolving from a vicinity of L_3.** In this part we illustrate the dynamical consequences of the behaviour of the unstable and stable manifolds of a NHIM: the centre manifold $W^c(L_3)$ of the libration point L_3 in the 3D restricted three-body problem. See [39] for equations and motivation, related to the role that the manifolds play in the practical confinement of the motion in a

large vicinity of the $L_{4,5}$ libration points. The selected values of the mass parameter and the Jacobi constant C are $\mu = 0.0002$ and $C = C^* = 2.95998466228$.

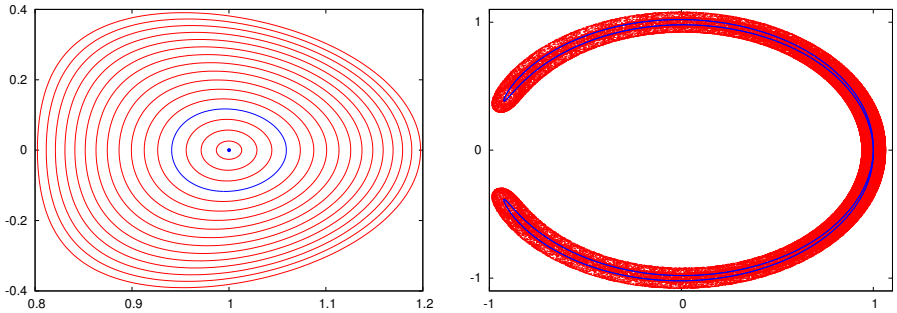

FIGURE 25. Left: Invariant curves on the section $\Sigma = \{z = 0, \dot{z} > 0\}$ lying on $W^c(L_3)$ at the Jacobi level C^*. Right: Starting close to the blue curve in the left plot, the projections on (x, y) of the first 10^5 Poincaré iterates are shown. For reference a part of the manifolds of the vertical Lyapunov p.o. is displayed in blue.

The Figure 25 left shows several of the invariant curves in Σ (2D tori in phase space) contained in $W^c(L_3)$ on the level C^*. The so-called vertical Lyapunov p.o. is marked as a blue dot. The planar Lyapunov p.o., contained in Σ, is located slightly outside the outer displayed invariant curve. Taking an initial point close to the curve shown in blue, the Poincaré iterates move along the red cloud shown in Figure 25 right. At the successive returns near $W^c(L_3)$ the points can move up (i.e., to the domain $y > 0$) or down, in a typical quasirandom way. For reference the initial parts of $W^{u,s}$ for the vertical Lyapunov p.o. are shown in blue.

To give evidence of diffusion, with the quasirandom passages near different invariant curves as the ones shown in Figure 25 left, the Figure 26 shows the evolution of the successive passages through a narrow 3D slice, near $x = 0$, inside Σ when we continue the iterations for the orbit partially shown in Figure 25 right. Note the strong contrast with Figure 19.

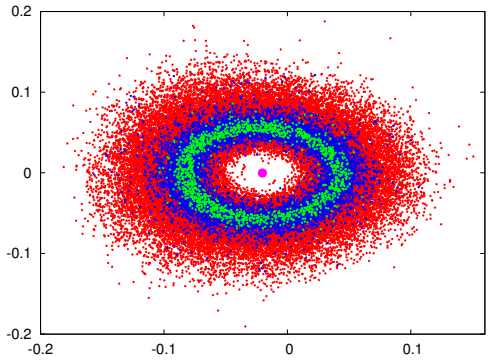

FIGURE 26. Passages through a narrow slice near $x = 0$ of the Poincaré iterates of an initial point near the blue curve in Figure 25 left. The points in green, blue and red correspond to the passages after 10^5, 8×10^5 and 5×10^6 iterates, respectively.

We can question what happens when the number of iterates increases. To this end several points have been taken near $W^c(L_3)$ close to the point corresponding to the vertical Lyapunov p.o. Looking at the iterates, they visit, in a quasirandom way, the different invariant curves shown in Figure 25 left, as it was illustrated in Figure 26, until they approach the planar Lyapunov p.o. and a escape is produced. Here escape means: a) either the points go to the outer part (say, radius greater than 2 in the (x, y) projection), or b) the points come close to the central body (say, radius less than $1/2$). In all these cases this escape is preceded by a close approach to the secondary mass located at $(\mu - 1, 0, 0)$.

For concreteness the Figure 27 shows how many points, from a sample of 625, taken initially extremely close, have not yet escaped as a function of the number of iterates. Up to 10^9 iterates only 13 points have not yet escaped. This gives a strong evidence of the diffusion taking place on the problem, which ends in escape.

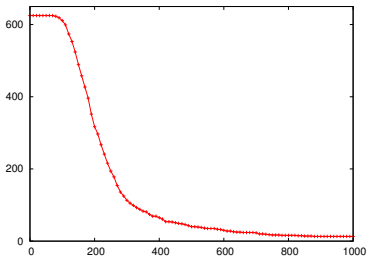

FIGURE 27. Number of non-escaping points as a function of the number of Poincaré iterates. The units in the number of iterates are expressed in millions.

It is worth to add that, during the trips of the iterates, one can observe the passage near 3D invariant tori. Due to the stickiness properties of these tori one checks that these passages, close to 3D tori, can occur for hundreds of millions of consecutive iterates. See [40] for additional information.

5. **Conclusions and Outlook.** Several simple Hamiltonian examples, resonant and non-resonant, in two and three degrees of freedom, have been studied around a totally elliptic, positive definite, fixed point located at the zero level of the energy h. The main goal has been to detect some measure of the set of points with chaotic behaviour and the dynamical objects responsible of the chaos. Cases ranging from a measure exponentially small in h to a large amount of chaos in the limit $h \to 0$ have been analyzed.

It has been stressed, for 2 dof, the role played by models like the separatrix map and the standard map or its variants. A similar task in the higher dimensional case, starting with the study in [44] and leading to models like the one introduced in [9] or its variants, should allow to derive careful quantitative estimates of the amount of chaos and to estimate the distance to resonance at which maximal dimension invariant tori exist.

Acknowlegments. The author has been supported by grants MTM2010-16425 (Spain) and 2009 SGR 67 (Catalonia). A massive usage has been made of the computing facilities of the Dynamical Systems Group of the Universitat de Barcelona.

REFERENCES

[1] V.I. Arnold and A. Avez, Problèmes ergodiques de la mécanique classique, Gauthier-Villars, Paris, 1967.

[2] H. Broer, R. Roussarie and C. Simó, *Invariant circles in the Bogdanov-Takens bifurcation for diffeomorphism*, Ergod. Th. & Dynam. Systems, **16** (1996), 1147–1172.

[3] H. Broer and C. Simó, *Hill's equation with quasi–periodic forcing: resonance tongues, instability pockets and global phenomena*, Bul. Soc. Bras. Mat., **29** (1998), 253–293.

[4] P. M. Cincotta and C. M. Giordano, C. Simó, *Phase space structure of multidimensional systems by means of the Mean Exponential Growth factor of Nearby Orbits (MEGNO)*, Physica D **182** (2003), 151–178.

[5] A. Delshams, V. Gelfreich, À. Jorba and T. Martínez-Seara, *Exponentially small splitting of separatrices under fast quasiperiodic forcing*, Comm. Math. Phys. **189** (1997), 35–71.

[6] A. Delshams, M. Gonchenko and P. Gutiérrez, *Exponentially small lower bounds for the splitting of separatrices to whiskered tori with frequencies of constant type*, Preprint,available at `http://www.ma.utexas.edu/mp_arc-bin/mpa?yn=14-5` .

[7] E. Fontich and C. Simó, *Invariant Manifolds for Near Identity Differentiable Maps and Splitting of Separatrices*, Ergod. Th. & Dynam. Systems, **10** (1990), 319–346.

[8] E. Fontich and C. Simó, *The Splitting of Separatrices for Analytic Diffeomorphisms*, Erg. Th. & Dyn. Systems, **10** (1990), 295–318.

[9] C. Froeschlé, *Numerical study of a four-dimensional mapping*, Astronom. and Astrophys., **16** (1972), 172–189.

[10] V. Gelfreich and C. Simó, *High-precision computations of divergent asymptotic series and homoclinic phenomena*, Discrete and Continuous Dynamical Systems B, **10** (2008), 511–536.

[11] V. Gelfreich, C. Simó and A. Vieiro, *Dynamics of 4D symplectic maps near a double resonance*, Physica D **243** (2013), 92–110.

[12] A. Giorgilli, A. Delshams, E. Fontich, L. Galgani and C. Simó, *Effective stability for a Hamiltonian system near an elliptic equilibrium point, with an application to the restricted three body problem*, Journal of Differential Equations, **77** (1989), 167–198.

[13] G. Gómez, J.M. Mondelo and C. Simó, *A Collocation Method for the Numerical Fourier Analysis of Quasi–periodic Functions. I: Numerical Tests and Examples*, Discrete and Continuous Dynamical Systems B, **14** (2010), 41–74.

[14] G. Gómez, J.M. Mondelo and C. Simó, *A Collocation Method for the Numerical Fourier Analysis of Quasi–periodic Functions. I: Analytical error estimates*, Discrete and Continuous Dynamical Systems B, **14** (2010), 75-109.

[15] M. Hénon and C. Heiles *The applicability of the third integral of motion: Some numerical experiments*, Astronom. J., **69** (1964), 73–79.

[16] H. Ito, *Non-integrability of the Hénon-Heiles system and a theorem of Ziglin*, Koday Math. J., **8** (1985), 129–138.

[17] J. Laskar *The chaotic motion of the solar system. A numerical estimate of the size of the chaotic zones* Icarus, **88** (1990), 266–291.

[18] F. Ledrappier, M. Shub, C. Simó and A. Wilkinson, *Random versus deterministic exponents in a rich family of diffeomorphisms*, J. Statist. Phys. **113** (2003), 85–149.

[19] A. Luque and J. Villanueva, *Quasi-Periodic Frequency Analysis Using Averaging-Extrapolation Methods*, SIAM J. Appl. Dyn. Syst. **13** (2014), 1, 1–46.

[20] R. Martínez and C. Simó, *Non-integrability of Hamiltonian systems through high order variational equations: Summary of results and examples*, Regular and Chaotic Dynamics, **14** (2009), 323–348.

[21] R. Martínez and C. Simó, *Non-integrability of the degenerate cases of the Swinging Atwood's Machine using higher order variational equations*, Discrete and Continuous Dynamical Systems A, **29** (2011), 1–24.

[22] N. Miguel, C. Simó and A. Vieiro, *From the Hénon conservative map to the Chirikov standard map for large parameter values*, Regular and Chaotic Dynamics, **18** (2013), 469–489.

[23] J.J. Morales-Ruiz, Differential Galois Theory and Non-Integrability of Hamiltonian systems, Progress in Mathematics **179**, Birkhäuser, 1999.

[24] J.J. Morales-Ruiz and J.P. Ramis, *Galoisian obstructions to integrability of Hamiltonian systems I*, Methods and Applications of Analysis, **8** (2001), 33–96.

[25] J.J. Morales-Ruiz and J.P. Ramis, *Galoisian obstructions to integrability of Hamiltonian systems II*, Methods and Applications of Analysis, **8** (2001), i97–112.
[26] J.J. Morales, J.P. Ramis and C. Simó, *Integrability of Hamiltonian Systems and Differential Galois Groups of Higher Variational Equations*, Annales Sci. de l'ENS 4^e série, **40** (2007), 845–884.
[27] J.J. Morales and C.Simó, *Non integrability criteria for Hamiltonians in the case of Lamé normal variational equations*, J. Diff. Equations, **129** (1996), 111–135.
[28] A. Morbidelli and A. Giorgilli, *Superexponential Stability of KAM Tori*, J. Statist. Phys, **78** (1995), 1607–1617.
[29] J. Moser, Stable and Random Motions in Dynamical Systems: With Special Emphasis on Celestial Mechanics, Princeton University Press, 1973.
[30] A.I. Neishtadt, *The separation of motions in systems with rapidly rotating phase*, Prikladnaja Matematika i Mekhanika, **48** (1984), 133–139.
[31] Ya. Pesin, *Characteristic exponents and smooth ergodic theory*, Russian Math. Surveys, **32** (1977), 55–114.
[32] J. Sánchez, M. Net and C. Simó, *Computation of invariant tori by Newton-Krylov methods in large-scale dissipative systems*, Physica D, **239** (2010), 123–133.
[33] C. Siegel and J. Moser, Lectures on Celestial Mechanics, Springer, 1971.
[34] C. Simó, *On the analytical and numerical approximation of invariant manifolds*, Modern methods in celestial mechanics, D. Benest and C. Froeschlé, editors, 285–330, Editions Frontières, Paris, 1990. (Also available at `http://www.maia.ub.es/dsg/2004/`).
[35] C. Simó, *Averaging under fast quasiperiodic forcing*, Integrable and chaotic behaviour in Hamiltonian Systems, I. Seimenis, editor, 13–34, Plenum Pub. Co., New York, 1994.
[36] C. Simó, *Invariant Curves of Perturbations of Non Twist Integrable Area Preserving Maps*, Regular and Chaotic Dynamics, **3** (1998), 180–195.
[37] C. Simó, *Global Dynamics and Fast Indicators*, Global Analysis of Dynamical Systems, H. W. Broer, B. Krauskopf and G. Vegter, editors, 373–390, IOP Publishing, Bristol, 2001.
[38] C. Simó and T. Stuchi, *Central Stable/Unstable Manifolds and the destruction of KAM tori in the planar Hill problem*, Physica D, **140** (2000), 1–32.
[39] C. Simó, P. Sousa-Silva and M. Terra, *Practical Stability Domains near $L_{4,5}$ in the Restricted Three-Body Problem: Some preliminary facts*, Progress and Challenges in Dynamical Systems, Springer Proceedings in Mathematics & Statistics Series, **54**, S. Ibáñez et al., editors, 367–382, Springer, 2013,
[40] C. Simó, P. Sousa-Silva and M. Terra, *Evidences of diffusion related to the centre manifold of L_3 in the 3D RTBP*. Work in progress.
[41] C. Simó and D. Treschev, *Stability islands in the vicinity of separatrices of near-integrable symplectic maps*, Discrete and Continuous Dynamical Systems B, **10** (2008), 681–698.
[42] C. Simó and A. Vieiro, *Resonant zones, inner and outer splittings in generic and low order resonances of Area Preserving Maps*, Nonlinearity, **22** (2009), 1191–1245.
[43] C. Simó and A. Vieiro, *Dynamics in chaotic zones of area preserving maps: close to separatrix and global instability zones*, Physica D, **240** (2011), 732–753.
[44] D. Treschev, *Multidimensional Symplectic Separatrix Maps*, J. Nonlinear Sci., **12** (2002), 27–58.
[45] S.L. Ziglin, *Branching of solutions and non-existence of first integrals in Hamiltonian mechanics I*, Funct. Anal. Appl., **16** (1982), 181–189.

Received

E-mail address: `carles@maia.ub.es`